Electronic Supplementary Material (ESI) for Energy & Environmental Science.

Binder-free High Silicon Content Flexible Anode for Li–ion Batteries

Hanwei Wang[a]†, Jinzhou Fu[b]†, Chao Wang[a], Jiangyan Wang[c], Ankun Yang[c], Caicai Li[a], Qingfeng Sun[a,]*, Yi Cui[c,] *, Huiqiao Li[b]*

[a]School of Engineering, Zhejiang A&F University, Hangzhou 311300, China

[b]State Key Laboratory of Materials Processing and Die & Mould Technology, School of Materials Science and Engineering, Huazhong University of Science and Technology (HUST), Wuhan 430074, China

[c]Department of Materials Science and Engineering, Stanford University, Stanford, California 94305, USA

*Corresponding author: Qingfeng Sun (qfsun@zafu.edu.cn), Yi Cui (yicui@stanford.edu) and Huiqiao Li (hqli@hust.edu.cn)

†These authors contributed equally to this work

Experimental

Characterization: The emission scanning electron microscope (SEM, Quanta FEG 250, FEI, USA) and transmission electron microscope (TEM, Tecnai G2 F20, FEI, USA) were used to observe the microstructure of the samples. The phase structure was determined by X-ray powder diffraction (XRD, D/MAX 2200, Rigaku, JPN). X-ray photoelectron spectroscopy (XPS) was conducted on a Thermo Scientific$^{\text{TM}}$ K-Alpha$^{\text{TM+}}$ spectrometer equipped with a monochromatic Al Kα X-ray source (1486.6 eV) operating at 100 W. The four-point probe method was used to measure the conductivity (Keithley 6220/2182A; Tektronix Co, USA). Nitrogen adsorption-desorption isotherms was measured on a Micromeritics Tristar 3000 system using vacuum-degassed samples at 77.4 K. The content of composites was studied by Thermogravimetric analysis (TGA, Thermal Analysis Instruments, Burlington, MA, USA). Raman spectra (LabRAM HR800, JY, Horiba) were collected with an excitation wavelength of 514.5 nm. Ultrasonic Cell Disruption System (JY99-IIDN, Ningbo Scientz Biotechnology Co. Ltd, China) with 650 watts of power was used to prepare and disperse the samples. The obtained samples were freeze-drying by a freezer dryer (SCIENTZ-18ND, Ningbo Scientz Biotechnology Co. Ltd, China).

Mechanical modelling. The geometrical model and its mesh are shown as following:

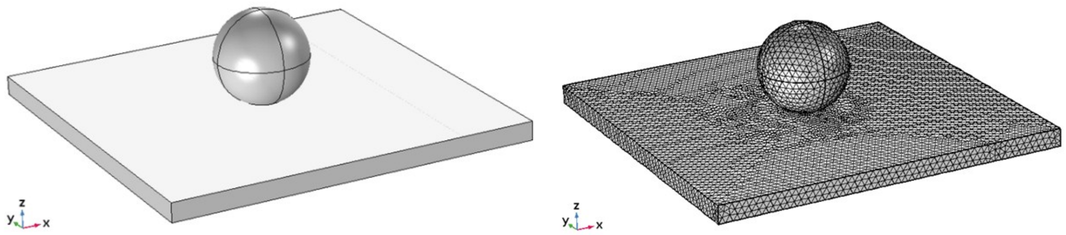

The silicon material model endowed to the particle with a density of 2329 kg/m^3, an elastic modulus of 170 GPa and a Poisson ratio of 0.28. The nanosheet used the cellulose material model with a density of 1760 kg/m^3, an elastic modulus of 60MPa and a Poisson ratio of 0.25. The method of transient analysis was used to calculate the process. The time was calculated in 30 seconds and the time step was 0.5 seconds. In combination with the nonlinear Newton iteration method, the direct strong coupling solver was used to calculate the result (the convergence factor was 0.01).

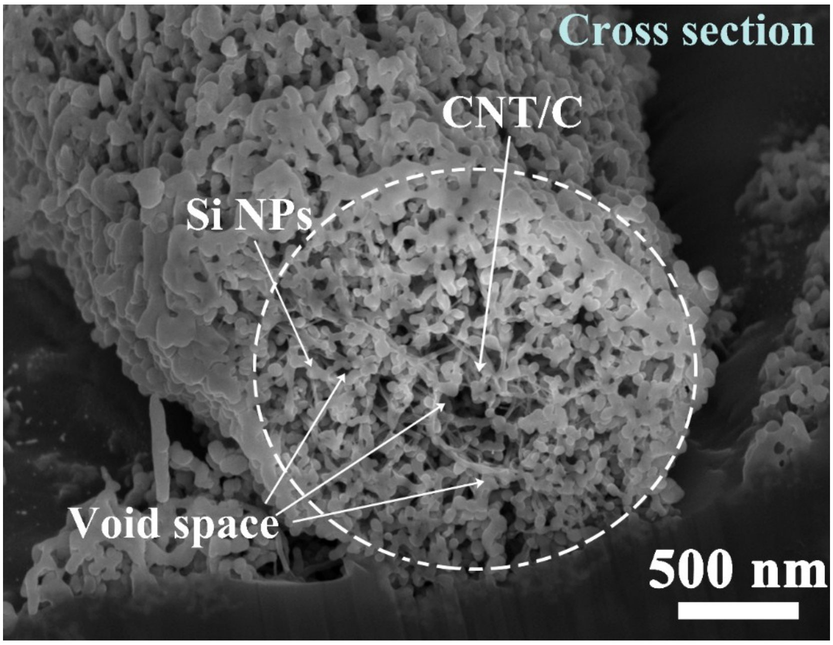

Figure S1. Dual-beam Focused Ion Beam (FIB) analysis and cross-sectioned SEM image of the Si@CNT/C-microscroll. The cross-sectioned image of the microscroll was provided by Dual-beam Focused Ion Beam (FIB) measurement. The FIB cutting is performed in vertical, and the corresponding SEM image indicates that the inside of the microscrolls have pores.

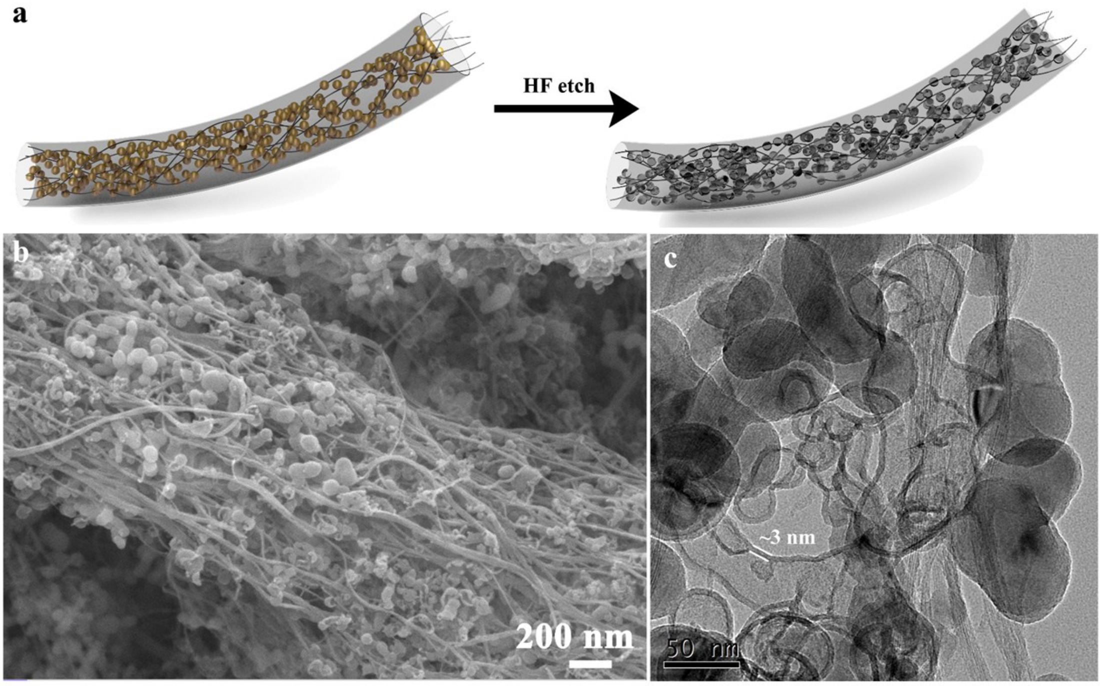

Figure S2. (a) The schematic scheme for the structure change of Si@CNT/C-microscrolls etched by HF before and after. **(b, c)** SEM and TEM images of the Si@CNT/C-microscrolls etched by HF. It is clearly seen that most silicon nanoparticles have been etched after HF treatment, remaining thin carbon shell (thickness: ~3 nm) and cross-linked CNT/C frameworks in the microscrolls. The formation of carbon shell was derived from the pyrolysis of cellulose coated on the surface of silicon.

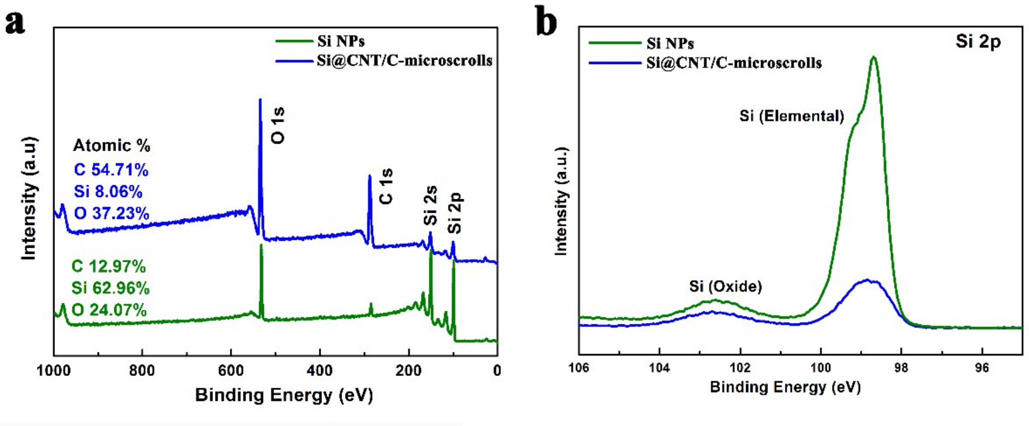

Figure S3. (a) XPS survey and **(b)** high-resolution XPS spectra of Si 2p peaks of the Si NPs and Si@CNT/C-microscrolls. As determined by XPS, the atomic percentage of Si in Si@CNT/C-microscrolls is extremely low (8.06%) in comparison with the corresponding content in pure Si (62.96%). It is also a strong evidence for a compact coverage of carbon in the surface of the microscrolls, considering the fact that the penetration depth of X-ray photoelectrons is merely several nanometers. The results of X-ray photoelectron spectroscopy (XPS) analysis (**Figure S3**) indicate compact coverage of carbon on the surface of the microscrolls, which is important for limiting the majority of SEI formation to the outer surface of the microscrolls and providing an enough conductivity.

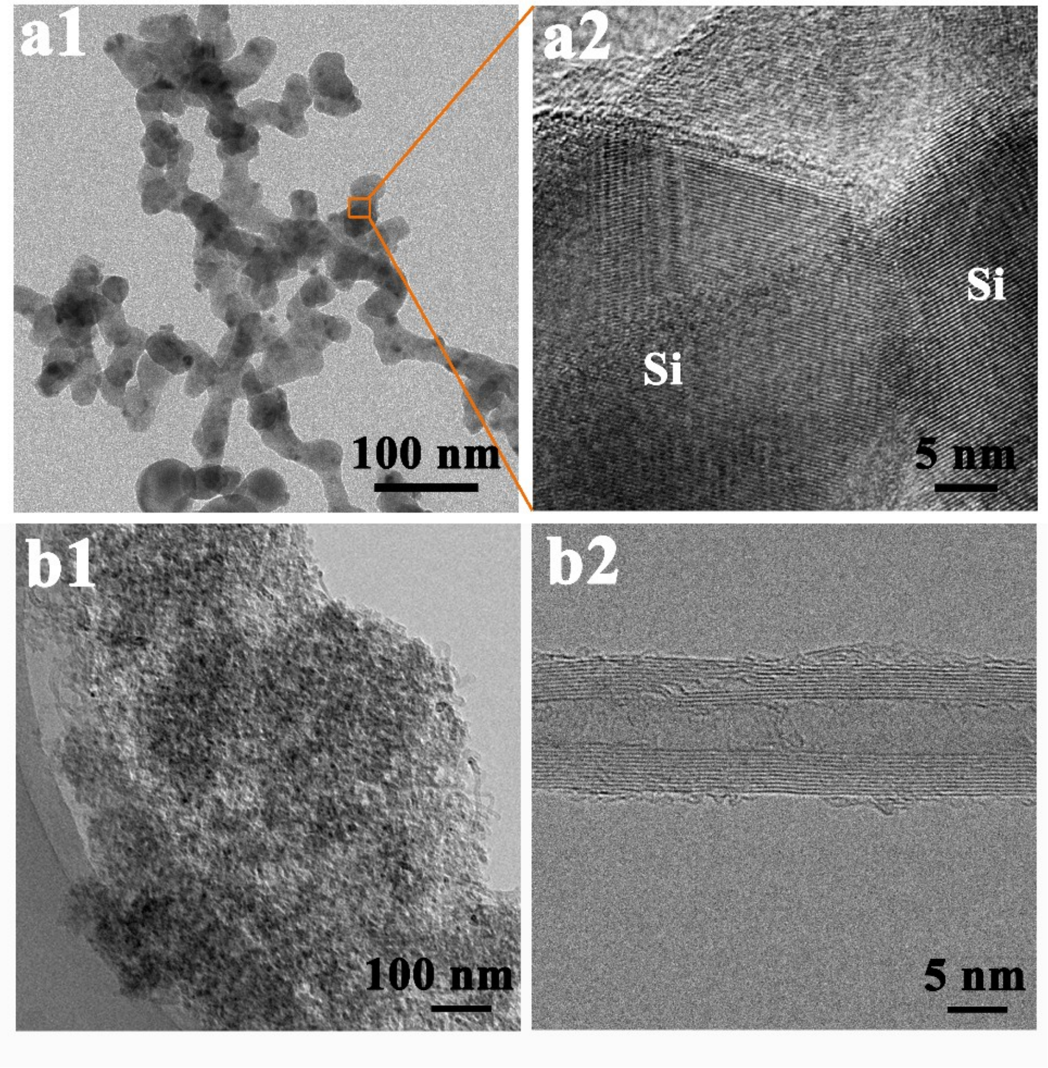

Figure S4. TEM images of **(a)** Si NPs and **(b)** CNT.

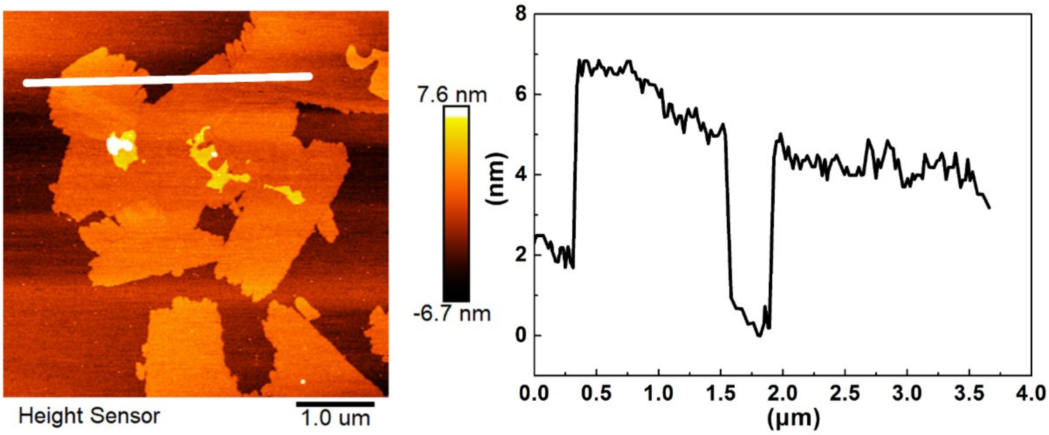

Figure S5 AFM images of cellulose nanosheets. Apparently, the thickness of cellulose nanosheets is about 4 nanometers.

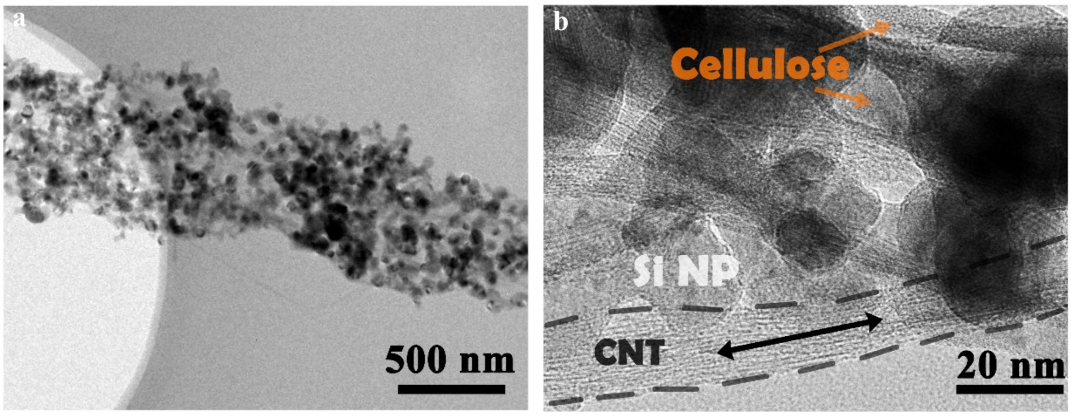

Figure S6. (a) TEM image of the Si@CNT/Cellulose microscrolls. **(b)** The magnified TEM image showing that the Si NPs and CNTs are fully coated by the cellulose in the microscrolls.

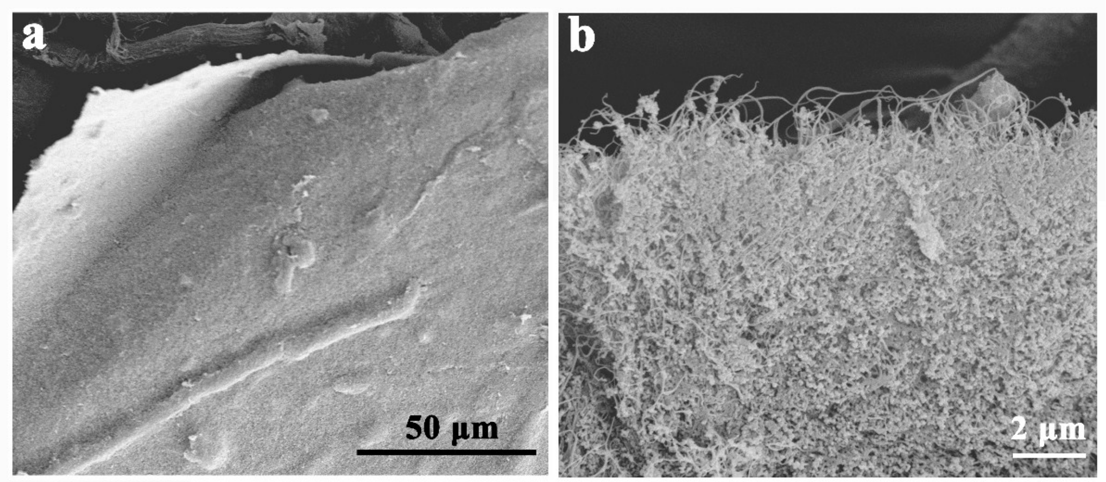

Figure S7. (a-b) SEM images of Si@CNT/Cellulose. This flake-like composite is observed from a drying treatment in the oven for frozen sample **without freeze-drying**, indicating freeze-drying process is important to the formation of the scrolls.

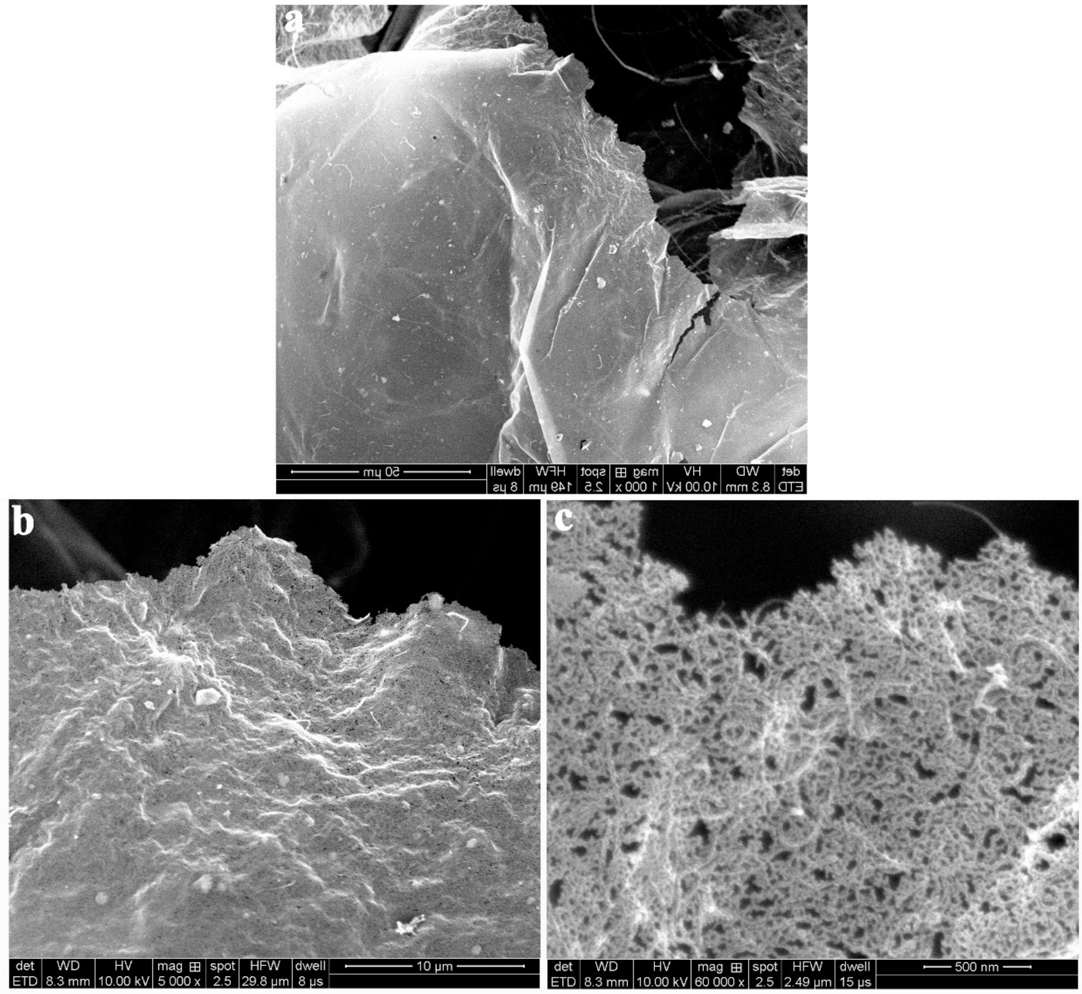

Figure S8. (a-c) SEM images of the CNT/Cellulose composite prepared by the same condition but **without Si NPs**. CNT/Cellulose composite without Si NPs shows a sheet-like structure, indicating that the existence of Si NPs induces the formation of the microscroll.

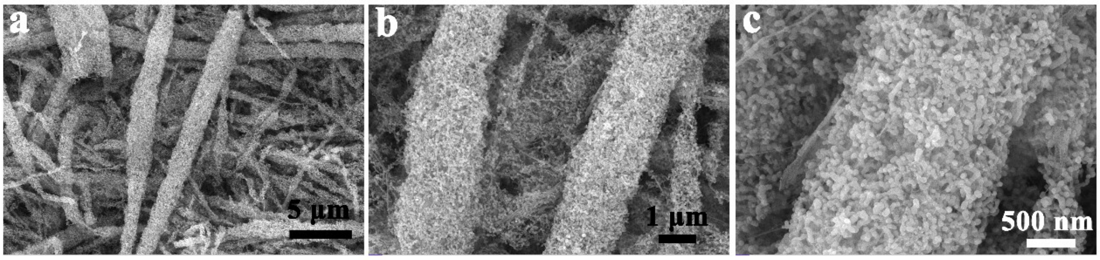

Figure S9. (a-c) SEM images of the Si/Cellulose composite. This Si/Cellulose composite with scroll structure is prepared by the same condition but **without CNTs**. It indicates that CNT has no influence on the formation of the scroll.

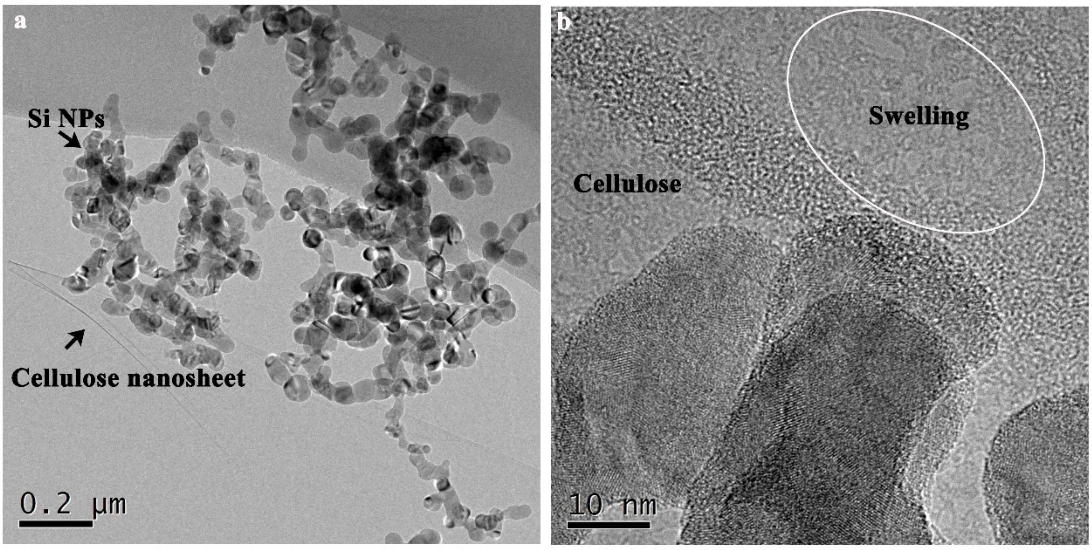

Figure S10. **(a)** TEM image and **(b)** its magnified images of the cellulose nanosheets and Si NPs mixed solution that was treated with ultrasonic.

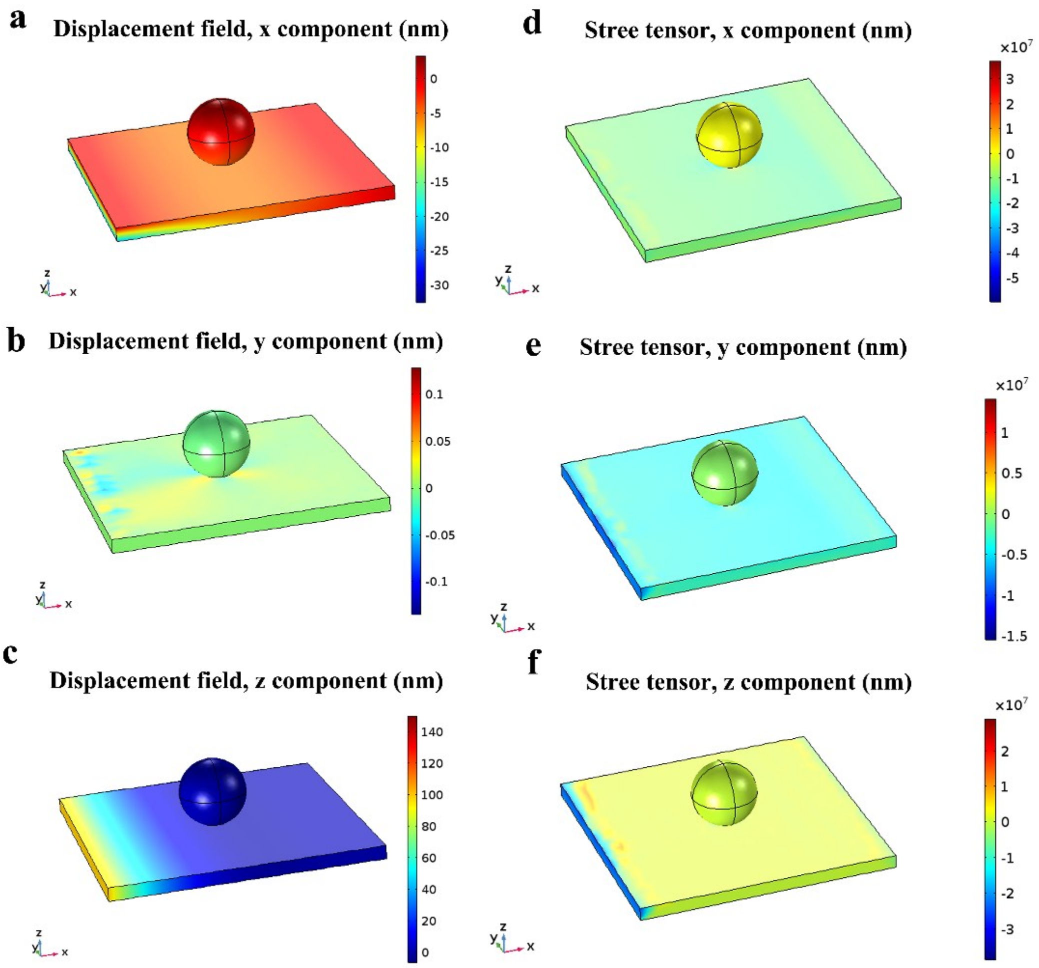

Figure S11. The displacement **(a-c)** and stress **(e-f)** distribution diagram in the x, y and z component corresponding to the final deformation in **Figure 2h.**

Table S1 The simulation results in the final deformation of cellulose nanosheet.

	Displacement X (nm)	Displacement Y (nm)	Displacement Z (nm)	Total dipacement (nm)	Stress X (MPa)	Stress Y (MPa)	Stress Z (MPa)
Positive	3	0.1	90	91	10	40	100
Negative	20	0.1	0		30	120	300

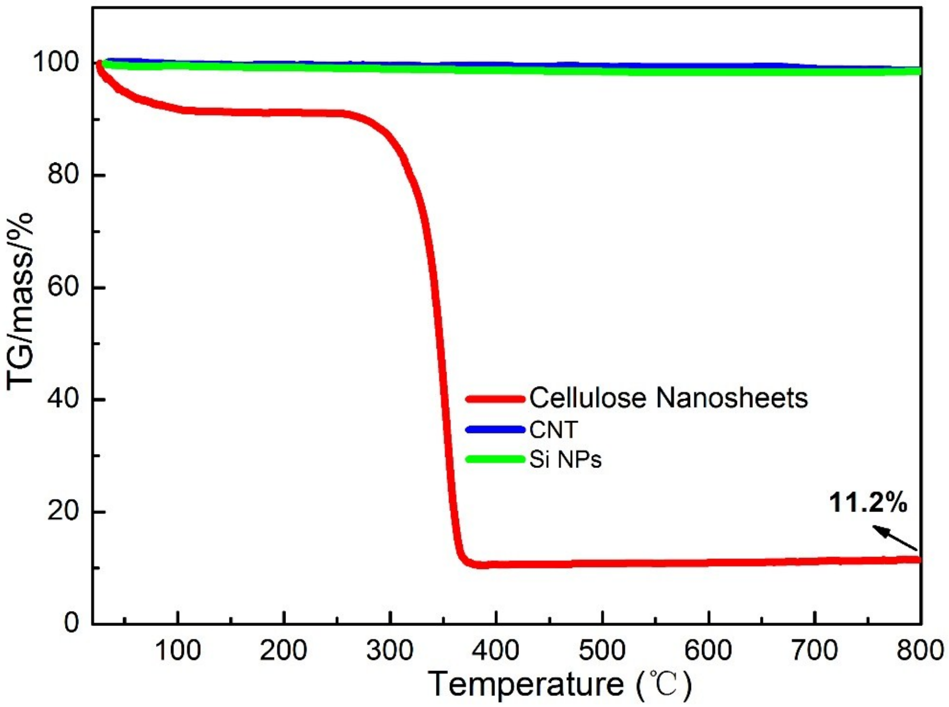

Figure S12. TG curves of cellulose nanosheets, CNT and Si NPs under Ar atmosphere. Among, mass loss only occurs in the cellulose nanosheets. After 800 °C, the weight of the cellulose residues (carbon) maintain at 11.2%.

Table S2. Fabrication of Si@CNT/C-microscrolls over wide conditions

CNT% [a]	**1.8%**	**8%**	**15%**	**21%**
Concentration (Si:Cel:CNT) [b]	1:1:0.02 g L^{-1}	1:1:0.1 g L^{-1}	1:1:0.2 g L^{-1}	1:1:0.3 g L^{-1}
Si% [a]	32%	74%	85%	92%
Concentration (Si:Cel:CNT) [b]	0.1:1:0.1 g L^{-1}	0.6:1:0.1 g L^{-1}	1.2:1:0.1 g L^{-1}	2.4:1:0.1 g L^{-1}

[a] Theoretical contents of CNT (W_{CNT}) and Si (W_{Si}) in the electrodes are calculated by the ratio of CNT weight and the theoretical weight of Si@CNT/Carbon electrode (W_1). Due to full utilization of these raw materials in the solution to form electrode after freeze-drying treatment, the concentrations of Si, CNT and Cellulose can be directly used to calculate their weight percentage in Si@CNT/Cellulose microscrolls (W_2). Here, assuming the concentration of CNT, cellulose and

Si are x, y and z, respectively. According to the TG results of the Si, CNT and cellulose (**Fig. S12**), the mass loss only appears in the cellulose during the annealing process. As a result, after annealing, the mass of CNT, cellulose derived carbon and Si is x, 11.2%*y and z, respectively. Thus, theoretical content of CNT (W_{CNT}) and Si (W_{Si}) in the Si@CNT/Carbon microscrolls can be described as following: W_{CNT}=x/(x+11.2%*y+z)*100%; W_{Si}=z/(x+11.2%*y+z) *100%.

[b] The concentrations of Si, cellulose nanosheets and CNTs are the preparation concentration of Si@CNT/Cellulose microscrolls in the original aqueous solution.

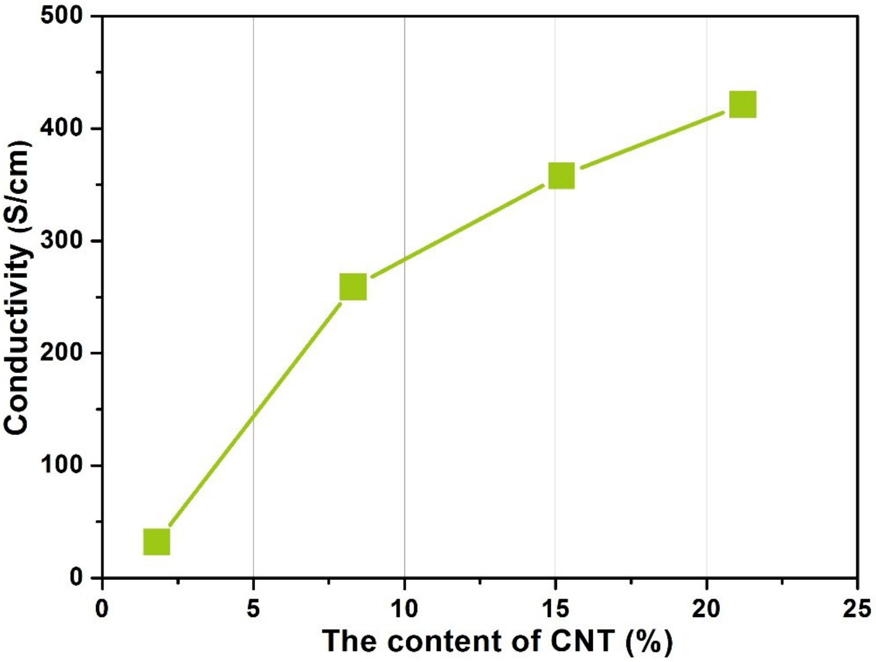

Figure S13. The conductivity of the Si@CNT/Carbon microscrolls with different CNT content.

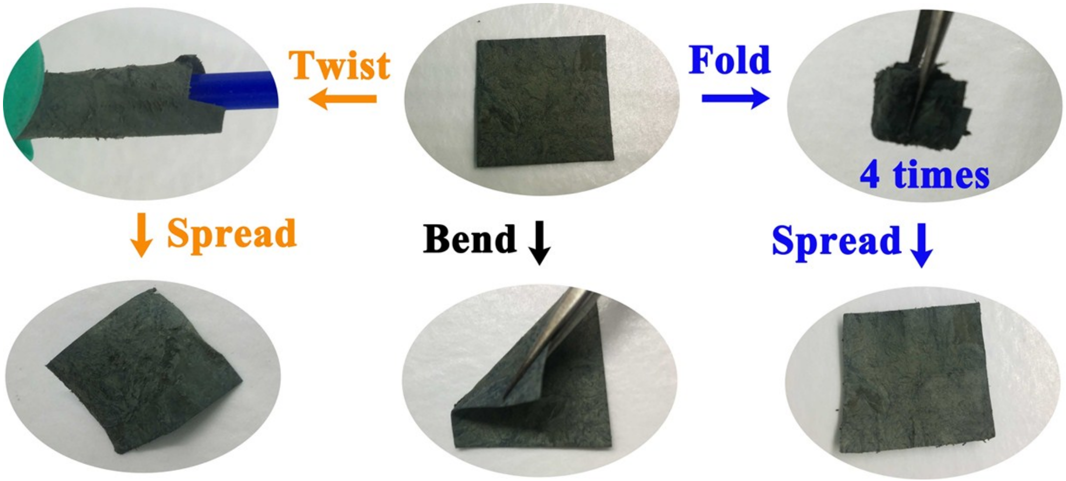

Figure S14 Flexibility tests of the microscroll electrodes.

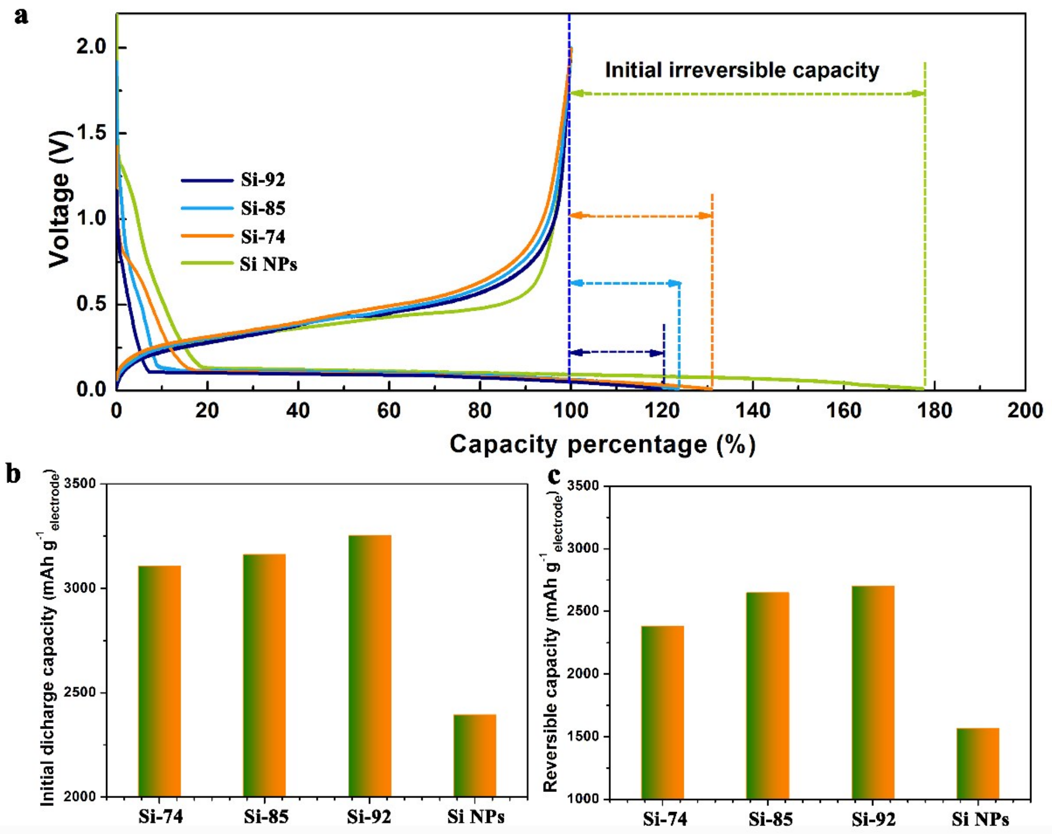

Figure S15. (a) First cycle voltage profiles of Si@CNT/C-microscroll with different Si content. The majority of the irreversible capacity is from the initial sloping part of the lithiation profile. The increased carbon contents in Si@CNT/C-microscroll electrode resulted in the lower CE, corresponding to the increased Li-ion consumption of more amorphous carbon. The pure Si NPs electrode possesses a second-largest initial sloping part but a lowest CE. It implies that in addition to more Li-ion consumption from its high surface, the partial irreversible capacity is related to their unstable structure compared to the Si@CNT/C-microscroll. **(b)** Initial delithiation capacity comparison. **(c)** Reversible capacity comparison.

Table S3. A summary of the performances of different Si-based anodes in comparison with the results in this work.

Description	**Mass loading (mg cm^{-2})**	**Si contents (wt%) in active materials**	**Si contents (wt%) in electrode (excel current collector)**	**Si contents (wt%) in electrode including current collector (Cu foil, 7 mg cm^{-2}) [a]**	**Reversible capacity (mAh g^{-1}) based on the electrode (include binder and conductive agent)**	**Highest Areal Capacity (mAh cm^{-2})**	**Reference**
Si@CNT/C-microscroll	0.8~2.2 mg cm^{-2}	92.2	92.2	92.2	2710 mAh g^{-1} **for whole electrode**	5.58 mAh cm^{-2}	**This work**
Silicon-nanolayer-embedded graphite	6.5 mg cm^{-2}	9	8.622	4.2	495 mAh g^{-1} at 0.5 C	>3.3 mAh cm^{-2}	[1]
Si/carbon pomegranate anodes	0.2 - 3.12 mg cm^{-2}	77	61.6	22	1040 mAh g^{-1} at 30 mA g^{-1} for Si/C	3.7 mAh cm^{-2}	[2]
Si/C Sphere	1.2 mg	30	18	4	961 mAh g^{-1} at 400 mA g^{-1}	/	[3]

	cm^{-2}						
Mesoporous silicon	1.0-2.0 mg cm^{-2}	60	48	12.6	880 mAh g^{-1} at 100 mA g^{-1}	/	4
Silkworm cocoon-like silicon/Carbon	/	78.3	66.55	/	1844 mAh g^{-1} at 500 mA g^{-1}	/	5
Si/C/SiOC	~2 mg·cm^{-2}	18	15.3	3.9	510 mAh·g^{-1} at 72 mA g^{-1}	0.35 mAh cm^{-2} under 2.38 mg cm^{-2}	6
Hierarchical carbon-coated metallurgical Si	0.5 mg/cm^{2}	95	66.5	6.1	1660 mAh·g^{-1} at 400 mA g^{-1}	/	7
flexible silicon and graphene/ carbon nanofibers	/	47	47	47	2002 mAh·g^{-1} at 700 mA g^{-1}	/	8
Si@void@C nanofibers	2 mg/cm^{2}	58	34.8	11.2	641 mAh·g^{-1} at 100 mA g^{-1}	~2 mAh cm^{-2}	9
Porous Silicon Particles	2.36 mg cm^{-2}	100	60	33.5	1920 mAh·g^{-1} at 500 mA g^{-1}	/	10
SiOx/C	3.5	30	27	9.6	585 mAh·g^{-1}	/	11

	mg cm^{-2}				at 130 mA g^{-1}		
carbon@void@silica/binder	0.2 mg cm^{-2}	/	60	/	1320 mAh·g^{-1} at 100 mA g^{-1}	0.44 mAh cm^{-2}	12
Double carbon shells coated Si nanoparticles	/	70.5	56.4	/	~1240 mAh·g^{-1} at 0.5 C	/	13
Amorphous TiO_2/Si	0.621 mg/cm^2	89	53.4	6.9	2060 mAh·g^{-1} at 140 mA g^{-1}	2.131 mAh cm^{-2}	14
Graphdiyne/Si/Cu	0.64-1.28 mg cm^{-2} for Si	30~40 wt % Free-standing	30~40 wt %	30~40 wt %	~1230 mAh·g^{-1} at 0.2 A g^{-1}	4.8 mAh cm^{-2}	15
Si/C	/	35	29.75	/	912 mAh·g^{-1} at 100 mA g^{-1}	/	16
SiOC/graphene composite paper	2 mg cm^{-2}	41.86	32.65	32.65	702 mAh·g^{-1} at 100 mA g^{-1}	1.4 mAh cm^{-2}	17
Si/C-graphite	~5 mg cm^{-2}	10	7.5	3.7	487.5 mAh·g^{-1} at 0.4 mA cm^{-2}	3 mAh cm^{-2}	18
FeCuSi	~1 mg cm^{-2}	70	56	8.5	1029 mAh·g^{-1} at 420 mA g^{-1}	3.4 mAh cm^{-2}	19

[a] Silicon content (wt%) in electrode including current collector (Cu foil, 7 mg cm^{-2}) is calculated according to equation as follows:

$W_{Si}=m_{Si}/(m_{Si\text{-based material}}+m_{conductive\ additive}+m_{binder}+m_{current\ collector}+m_{others})*100\%$

where W_{Si} is the Silicon content (wt%) in electrode including current collector (Cu foil, assuming 7 mg cm^{-2}), m_{Si}, $m_{Si\text{-based material}}$, $m_{conductive\ additive}$, m_{binder}, $m_{current\ collector}$ and m_{others} are the mass of silicon, silicon-based active material, conductive additive, binder, current collector and other additives in the electrode.

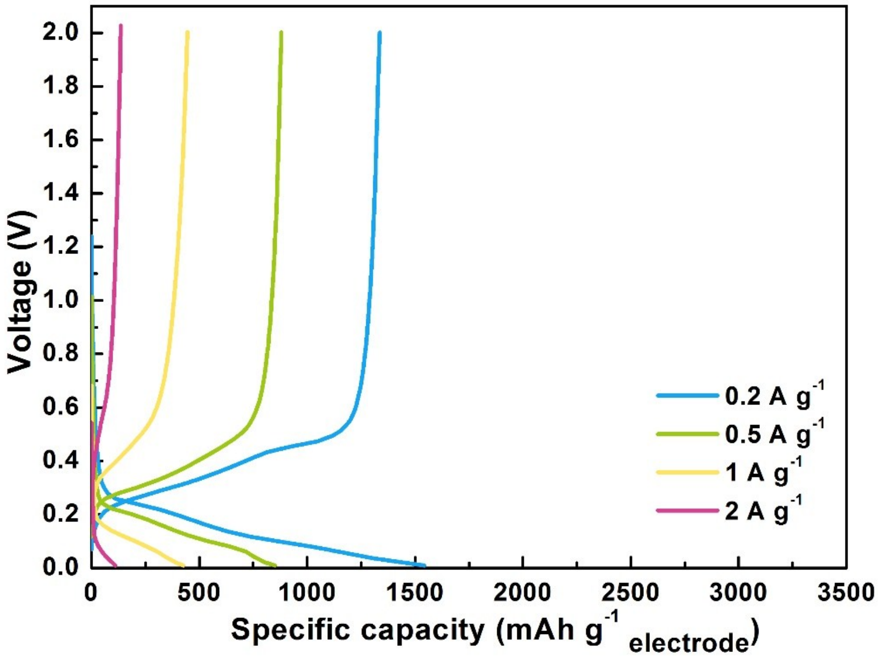

Figure S16. Voltage profiles of the pure Si NPs electrode cycled at various rates from 0.2 A g^{-1} to 5 A g^{-1} in the potential window of 0.01 to 2 V versus Li/Li^{+}. After deducting the mass of the carbon black and binder (50%), the capacity of Si NPs in pure Si NPs electrode is 3086 mAh g^{-1} at 0.2 A g^{-1}. After deducting the contribution of CNT/C, the capacity with respect to silicon in Si@CNT/C-microscroll electrode is as high as 3156 mAh g^{-1} at 0.2 A g^{-1}.

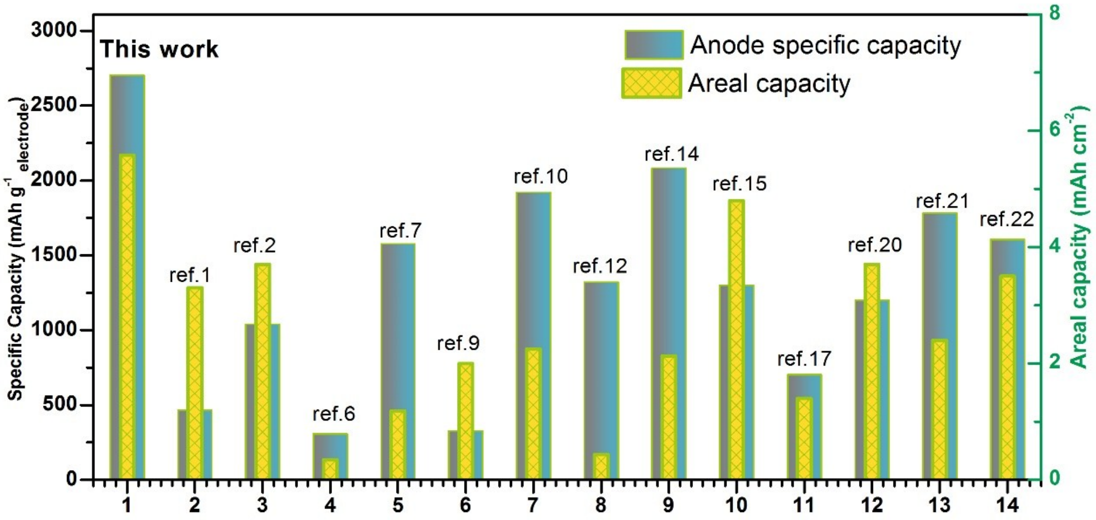

Figure S17. Performance comparison with the Si anodes by prevailing method in literatures [1, 2, 4, 6, 7, 9, 10, 12, 14, 15, 17, 20-22].

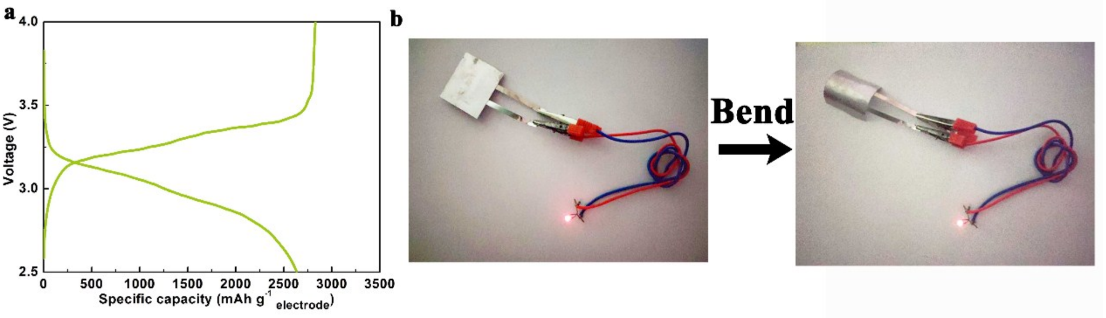

Figure S18 (a) Second charge/discharge voltage–capacity curves. **(b)** Photo of the cell lighting a LED indictor with and without bending.

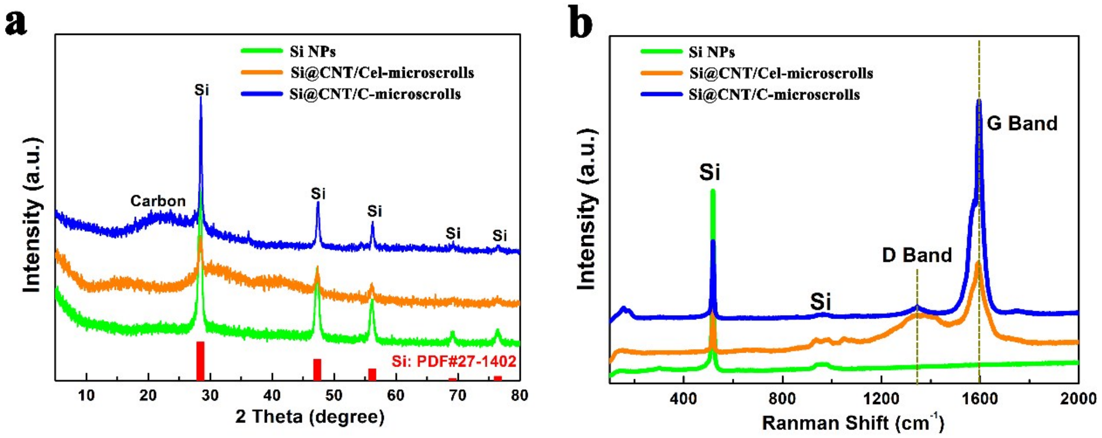

Figure S19. **(a)** XRD patterns and **(b)** Raman spectra of the Si NPs, Si@CNT/Cel-microscrolls and Si@CNT/C-microscrolls.

Reference

1. M. Ko, S. Chae, J. Ma, N. Kim, H. W. Lee, Y. Cui and J. Cho, *Nature Energy*, 2016, **1**, 16113.
2. L. Nian, L. Zhenda, Z. Jie, M. T. Mcdowell, L. Hyun-Wook, Z. Wenting and C. Yi, *Nature Nanotechnology*, 2014, **9**, 187-192.
3. M.-G. Jeong, H. L. Du, M. Islam, J. K. Lee, Y.-K. Sun and H.-G. Jung, *Nano Letters*, 2017, **17**, 5600-5606.
4. N. Kim, H. Park, N. Yoon and J. K. Lee, *ACS Nano*, 2018, **12**, 3853-3864.
5. F.-H. Du, Y. Ni, Y. Wang, D. Wang, Q. Ge, S. Chen and H. Y. Yang, *ACS Nano*, 2017, **11**, 8628-8635.
6. D. Vrankovic, M. Graczyk-Zajac, C. Kalcher, J. Rohrer, M. Becker, C. Stabler, G. Trykowski, K. Albe and R. Riedel, *ACS Nano*, 2017, **11**, 11409-11416.
7. C. Shen, X. Fang, M. Ge, A. Zhang, Y. Liu, Y. Ma, M. Mecklenburg, X. Nie and C. Zhou, *ACS Nano*, 2018, **12**, 6280-6291.
8. J. Zhu, T. Wang, F. Fan, L. Mei and B. Lu, *ACS Nano*, 2016, **10**, 8243-8251.
9. Y. Han, J. Zou, Z. Li, W. Wang, Y. Jie, J. Ma, B. Tang, Q. Zhang, X. Cao, S. Xu and Z. L. Wang, *ACS Nano*, 2018, **12**, 4835-4843.
10. M. Sohn, D. G. Lee, H.-I. Park, C. Park, J.-H. Choi and H. Kim, *Advanced Functional Materials*, 2018, **28**, 1800855.
11. Q. Xu, J.-K. Sun, Y.-X. Yin and Y.-G. Guo, *Advanced Functional Materials*, 2018, **28**, 1705235.
12. Y. Liu, Z. Tai, T. Zhou, V. Sencadas, J. Zhang, L. Zhang, K. Konstantinov, Z. Guo and H. K. Liu, *Advanced Materials*, 2017, **29**, 1703028.
13. S. Chen, L. Shen, P. A. van Aken, J. Maier and Y. Yu, *Advanced Materials*, 2017, **29**, 1605650.
14. J. Yang, Y. Wang, W. Li, L. Wang, Y. Fan, W. Jiang, W. Luo, Y. Wang, B. Kong, C. Selomulya, H. K. Liu, S. X. Dou and D. Zhao, *Advanced Materials*, 2017, **29**, 1700523.

15. H. Shang, Z. Zuo, L. Yu, F. Wang, F. He and Y. Li, *Advanced Materials*, 2018, **30**, 1801459.
16. H. Su, A. A. Barragan, L. Geng, D. Long, L. Ling, K. N. Bozhilov, L. Mangolini and J. Guo, *Angewandte Chemie International Edition*, 2017, **56**, 10780-10785.
17. L. David, R. Bhandavat, U. Barrera and G. Singh, *Nature Communications*, 2016, **7**, 10998.
18. X. Li, P. Yan, X. Xiao, J. H. Woo, C. Wang, J. Liu and J.-G. Zhang, *Energy & Environmental Science*, 2017, **10**, 1427-1434.
19. S. Chae, M. Ko, S. Park, N. Kim, J. Ma and J. Cho, *Energy & Environmental Science*, 2016, **9**, 1251-1257.
20. S. Choi, T.-w. Kwon, A. Coskun and J. W. Choi, *Science*, 2017, **357**, 279-283.
21. Z. Zhang, Z. L. Wang and X. Lu, *ACS Nano*, 2018, **12**, 3587-3599.
22. D. Lin, Z. Lu, P.-C. Hsu, H. R. Lee, N. Liu, J. Zhao, H. Wang, C. Liu and Y. Cui, *Energy & Environmental Science*, 2015, **8**, 2371-2376.